Acta Astronautica 190 (2022) 273–282

Contents lists available at ScienceDirect

Acta Astronautica

journal homepage: www.elsevier.com/locate/actaastro

Research paper

Stereovision for surveillance of Earth orbiting objects: Two methods and their validation with synthetic data

Andrea Cavagna [a,c], Massimo Cencini [a], Stefania Melillo [b,c,*], Leonardo Parisi [b,c,*], Fabrizio Piergentili [d], Fabio Santoni [e], Alessandro Sozza [a,f]

[a] CNR–ISC (National Research Council - Institute for Complex Systems), Rome, Italy
[b] CNR–ISC (National Research Council - Institute for Complex Systems) UOS Sapienza, Rome, Italy
[c] Department of Physics Sapienza University of Rome, Rome, Italy
[d] Department of Mechanical and Aerospace Engineering (DIMA) Sapienza University of Rome, Rome, Italy
[e] Department of Astronautics, Electric and Energy Engineering (DIAEE) Sapienza University of Rome, Rome, Italy
[f] Laboratoire de Physique, École Normale Supérieure de Lyon, Lyon, France

ARTICLE INFO

Keywords:
Space Surveillance
Space debris
Triangulation
3D reconstruction

ABSTRACT

Due to the new trend of space economy and to the resulting increase of space objects, Space Surveillance and Space Traffic Management are becoming essential to reduce the risk of in-orbit collisions and of potential on Earth damages from uncontrolled re-entries. Ground based optical observations, where cameras are coupled with telescopes, represent an invaluable resource for space debris monitoring and tracking. Observations from one single site may provide angular celestial coordinates of a space object, but they must be supplemented with filters and astrodynamic models to provide an estimate of the object trajectory. An alternative approach is the use of multi-site optical observations, where images of the same portion of sky collected with different cameras are matched to retrieve the $3D$ instantaneous position of space objects without the need of a priori knowledge of the object orbit parameters. Therefore, multi-site observations are extremely convenient to track uncontrolled Earth re-entry and close approach, where the orbit parameters are generally not stable. Here we focus on two-cameras systems and we discuss the use of two triangulation methods: one based on analytic geometry, the other one based on projective geometry. As a proof-of-concept, we compare the performance of the two methods in terms of accuracy in the $3D$ reconstruction on synthetic images that reproduce the night sky – including orbiting objects and stars – from different locations. To simulate realistic data sets, we produced images taking into account the effect of refraction and annual aberration on the stars, and we added gaussian noise to the position of the stars and of the space objects on the images. The comparison between the two methods shows that they are both valuable, with the projective method being more robust against noise.

1. Introduction

The massive growth of space debris of last decades as well as the recent advent of megaconstellations extremely increased the risk of in orbit collisions and of on Earth damages due to uncontrolled re-entry. To deal with these risks a Space Traffic Management system, including rules on end of life operations and infrastructures and techniques for orbiting object trajectory measurement, is needed and its development is underway worldwide, [1]. In this framework, surveillance and tracking activities exploiting ground based measurement systems (i.e. radar, laser and optical observatories) play a major role, and these systems are continuously evolving to face the challenge of monitoring fast moving, faint man made objects.

Optical systems, consisting of cameras connected to telescopes, have been dedicated to this purpose for more than 20 years [2,3]. They are by far the most common and most accessible instrument for ground-based observations. When compared to laser and radar systems, cameras offer a higher sensitivity at larger distances [4], due to the lower signal attenuation, at lower cost in terms of hardware and, being fully passive instruments, also in terms of power consumption.

Optical observations from one single site provide the angular celestial coordinates of a target, which must be further analyzed to estimate the object trajectory through sequential or batch filters, including astrodynamical model, [5]. Thus, the reliability of the reconstructed trajectory is largely influenced by the mathematical model and by

* Corresponding authors at: CNR–ISC (National Research Council - Institute for Complex Systems) UOS Sapienza, Rome, Italy.
E-mail addresses: stefania.melillo@cnr.it (S. Melillo), leonardo.parisi@cnr.it (L. Parisi).

https://doi.org/10.1016/j.actaastro.2021.10.011
Received 8 July 2021; Received in revised form 17 September 2021; Accepted 6 October 2021
Available online 15 October 2021

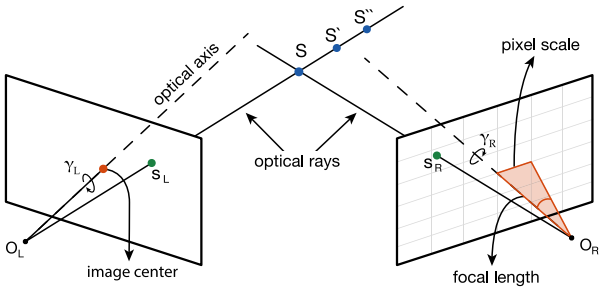

Fig. 1. Stereo vision. Information from only one camera are not sufficient to retrieve the range of an object: from the left camera point of view the three objects S, S' and S'' belong to the same optical ray, hence they correspond to the same $2D$ point, s_L, on the left image. To overcome this range ambiguity we need to match the information between two cameras. The object S lies at the intersection of the two optical rays (one for each camera) defined by its images, s_L and s_R, on the two sensors. The pixel scale and the focal length are related by a linear relation, such that the pixel scale represents the angle span one pixel and it is then higher the lower the focal length.

the accuracy of the measurements in terms of precision, quantity, distribution along the orbit and geometry of the instantaneous observation. This limitation may be overcome by triangulation, namely by matching information from two cameras simultaneously shooting at the same portion of the sky from two different locations [6–8], see Fig. 1. The 3D reconstructed position obtained via triangulation gives more information on the target state than a radar or a laser, which may only measure its range. This makes multi-site optical observations a powerful instrument when dealing with Earth re-entry or close approach, where an instantaneous target position fix, not based on dead reckoning methods, can greatly improve the number of feasible options to avoid collision damages or to better determine the point of impact on the Earth in the re-entry phase.

In this paper we discuss the $3D$ reconstruction of orbiting object positions via multi-site optical observations with the aim of validating the accuracy of two different methods: i. **the analytic method** that exploits direct triangulation in the $3D$ Euclidean space; ii. **the projective method**, commonly employed in computer vision [9], which performs triangulation in the $3D$ projective space.

As a proof-of-concept and to have maximal control on the procedures, we evaluate the performance of the two methods on synthetic data that reproduce images of the night sky from two different observation sites. In particular, we considered two locations corresponding to 5SLab network [10], so to have a synthetic data set to benchmark forthcoming field observations. In order to make a quantitative assessment of the reconstruction accuracy, we generated a number of synthetic night sky images of stars (varying both the elevation and the azimuth) using the Tycho-2 catalogue and including both the effect of annual aberration and atmospheric refraction. For each night-sky we considered hundreds of 3D positions in the field of view at different altitude from the Earth surface within the LEO region. These data points represent the positions of putative orbiting objects imaged on the virtual camera sensors.

We found that both methods give excellent results in terms of the $3D$ reconstruction accuracy on these sets of noise-free data, producing negligible error (mainly due to aberration and refraction) though with a trend with the (angular) elevation of the objects, such that the error increases when the elevation decreases, due to both the effect of refraction and tendency to parallelism of the optical axis of the two cameras. The accuracy of the two methods is comparable, except for very low elevation where the analytic method gives the best performance.

However noise free data are not realistic. The effect of noise on real images is essentially a $2D$ mis-positioning of the objects and of the stars on the camera sensor. Therefore we produced a second set of data with three different noise configurations: (i) adding noise only on the 2D positions of the objects; (ii) adding noise only on the 2D positions of the stars; (iii) adding noise both on objects and stars. The noise on the $2D$ position of the object produces the highest error and, unlike the noise free tests, the performance of the two methods are comparable even for low object elevation. With the addition of noise on the stars we also observe an error higher than in the noise-free condition, with the projective method giving better performance than the analytic one, hence suggesting that the projective method might be more robust against errors on the star field.

In order to test the method in a more realistic, yet synthetic, setting, we propagated a few satellites (in the LEO region) with the SGP4 model (Simplified General Perturbation) and the associated libraries from Vallado [11], we identified the stars visible from the two observatories and we generated synthetic images of the satellite passage. Then we tested the two methods on these data both in noise-free condition and with the addition of segmentation noise, confirming the performance of the two 3D-reconstruction methods in a more realistic setting.

The paper is organized as follows. In Section 2 we briefly describe the two reconstruction methods. In Section 3 we detail the procedure used to generate synthetic images. Section 4 is devoted to the tests and results of the reconstruction methods on the synthetic data. Summary and final considerations are presented in Section 5. Details on the methods and a few technical considerations are discussed in the Appendices.

2. Stereoscopic 3D reconstruction: two methods

The reconstruction of an object $3D$ position from a pair of images basically requires to define the two optical rays (one for each camera) where the object lies. For real images a preliminary astrometric and photometric analysis is needed to determine (from the images) the direction at which the cameras are pointing and to detect the stars and all the objects in the cameras field-of-view, through the so called segmentation process.

Astrometric estimates are based on solving the star-field, namely on identifying the stars in the images to define the portion of sky at which the cameras are pointing and, in particular, the RA/DEC of the image center, the rotation angle of the camera sensor with respect to the celestial North, and the pixel scale, i.e. the angular pixel size. To solve the star-field we used the Open Source program Astrometry-net [12]. Once astrometric measurements are obtained for both the cameras in the two different locations, they are used to estimate the geometry of the system and to define the two lines where the object lies, which are then used to reconstruct the object $3D$ position.

We implemented the two following methods (see Appendix A for details): i. **The analytic method** uses the astrometric parameters to retrieve the J2000 topocentric RA/DEC coordinates of the object, derived through Astropy. These coordinates are combined with the GPS position of the two observatories to estimate the parametric equation (in the J2000 reference frame) of the two optical rays passing by the object. The $3D$ reconstructed position is then obtained by finding (via minimization) the $3D$ point closest to the hypothetical rays intersection [9], working in the Euclidean space (see Appendix A.1 for the derivation). ii. **The projective method** uses the astrometric parameters to compute the cameras projective matrices, which define the geometry of the system in the $3D$ projective space. The projective matrices together with the pixel positions of the object in the two cameras are then used to estimate the direction of the optical rays passing by the object and its two images. Details on the method can be found in Appendix A.2.

While the two methods produce the same output, namely the J2000 $3D$ position of the object, they differ on how they process the input data, which indirectly implies a possible difference on the error propagation.

3. Generation of synthetic images

The procedure to generate the synthetic data can be broken onto the following steps:

1- Choice of the observation sites. While for synthetic data there is a great freedom in the choice of the observation sites, we chose to evaluate the performance of the two methods using two locations corresponding to observatories belonging to the 5SLab network: the REmote Space Debris Observation System (RESDOS) located in Rome and the Sapienza Coupled University Debris Observatory (SCUDO) in Collepardo, Italy.[1] This choice has the twofold benefit of simulating a realistic set-up and of producing a potential benchmark for our future experimental campaigns. For the sake of easy reading, in the following we will refer to the orbiting object as a satellite, but the entire procedure may be generalized to a generic object.

2- Generation of synthetic satellite positions. In order to test the sensitivity of the reconstruction method to a large number of parameters and configurations, we implement an algorithm to generate random satellite positions. We initially focus on one of the two cameras, namely the one in Rome, and we choose the direction where the camera is pointing by fixing the azimuth and elevation of its image center. We pick at random a pixel position of the object on the (virtual) camera sensor and fix its altitude. With these parameters we determine the $3D$ position of the object in the ECEF reference frame. Finally we back project the $3D$ position of the object onto the second camera, the one in Collepardo, as detailed in Appendix B. Note that with this procedure we are automatically producing images of objects that are simultaneously visible from the two observatories. As discussed below we also consider atmospheric refraction so that the reconstruction will be affected by an error. Since we limit the analysis to the LEO region we do not include time of light corrections to the satellite positions, as at these altitudes it can be neglected, [11]. Iterating this procedure, we can generate an ensemble of random satellite positions at different heights.

3- Computation of realistic satellite trajectory. Besides the random satellite points determined as described above, in order to work out realistic situations, we also computed the trajectory of an orbiting satellite through SGP4 model (Simplified General Perturbation) and the associated libraries from Vallado [11], initializing the model with the orbital data provided by the Norad Two-Line Elements (TLE) sets released by NASA. Geodetic and geographic constants of the Earth are provided by the WGS84 (World Geodetic System), a standard in cartography and satellite navigation including GPS, and by Earth Orientation Parameters (EOP) describing irregularities in the rotation of the Earth [13]. Once the satellite trajectory is computed, we identify the time window in which the satellite is visible from both observation sites. We require that the satellite is in the field of view of both cameras. Further, we impose that the Sun elevation is smaller than $-10°$ and that the satellite elevation is larger than $10°$ from both observatories. We sample the trajectory with time step given by the exposure time of cameras, typically 0.5 s. We record the details of the satellite passage, like azimuth and elevation (actually we use the apparent elevation as we include the effects of atmospheric refraction, see Appendix C), which will be used in the next steps of this procedure to generate the images, but also its J2000 $3D$ position, which will be used to estimate the reconstruction error during the evaluation tests.

4- Selection of the stars in the field of view. To identify and locate the stars that are visible from the two cameras, we use Tycho-2 catalogue that includes more than 2.5 million of stars and other astrophysical objects [14] (available at [15]). The catalogue provides equatorial coordinates (α, δ) in J2000, proper motion, magnitude, parallax and other information. Given the exact date and time, the angular coordinates of the optical axis and the sensor sizes, we identify the stars that should be imaged. In order to recreate realistic data sets, we apply stellar aberration in the position of star computed in J2000 frame of reference. Based on the motion of the observer, the aberration consists of three types: diurnal, due to daily rotation of the Earth around its axis, annual, due to the motion of the Earth around the Sun, and secular, due to the motion of the solar system. For stars sighting from the Earth ground, the main contribution is accounted by the annual aberration. Hence we neglect the others. For the sake of simplicity, we also do not include corrections due to proper motion, parallax, etc. since their effect is subdominant [16,11]. We transform the stars coordinates in the reference frame at the epoch of the image using precession and nutation. Finally we compute azimuth and elevation in the topocentric reference frame of the two sites.

5- Computation of the refraction correction. We take into account, on both stars and satellites, the unavoidable distortion due to the atmospheric refraction, which has the effect of deviating the rays of light coming from the observed objects. The magnitude of this deviation depends on several factors: the position of the object with respect to the zenith at the observer location, the wavelength of the light emitted by the objects and the atmospheric conditions such as temperature and pressure. Following [16], we simulate the refraction effect fixing the temperature at 10 °C and the pressure at 1010 mbar. For the sake of simplicity we do not take into account the effect of the different wavelengths, which is proved to be sub-dominant with respect to the effect of the object position [17,18], but we simulate the atmospheric refraction corresponding to the yellow light only. The small variations on the refracted positions due to the effect of different wavelengths may be considered as part of the noise that we add on the object positions, see Step 7 below.

In practice, given a pair of azimuth and elevation coordinates of an object in the topocentric coordinates of the observation sites, we compute the object apparent elevation, namely the elevation at which an observer on the Earth would see the object. Note that we apply the refraction correction also to the Az/El coordinates of the image center defined in Step 1, see Appendix C for further details on the refraction correction and its effects on the images.

6- Generation of the images. The pixel positions of the satellite and the stars on the virtual sensors of the two cameras are obtained from their azimuth and apparent elevation coordinates. Using the azimuth and apparent elevation of the image center and the camera pixel scale, we exploit the projection scheme described in Appendix B. Once the positions of stars and satellites are determined we derive a corresponding image and directly write them in FITS (Flexible Image Transport System) files. In *real* images of the night sky, depending on the telescope motion mode, the satellites or the stars or both satellites and stars appear as streaks of light. When this happens, the position of the streaked objects on the images can only be approximated as the centroid of the streak, with a consequent potential segmentation error. To keep the synthetic data as simple as possible, here we do not simulate this streaking effect and, for both the satellites and the stars, we produce point-like images. We take into account the effect of the streaks by directly adding noise, as described in Step 7 below, to the synthetic positions generated in Step 2.

7- Addition of noise. Our synthetic data does not exactly reproduce real images, not only because of the approximation we used in the computation of the atmospheric refraction, where we do not include the dependence on the wavelength (see Step 5 above), nor because of the point-like appearance of satellites and stars, where we do not consider streaked objects (see Step 6 above), but also because of several source of errors that affect real images and that cannot be properly simulated, among the others air turbulence, optic distortion and dark current. All these factors may be seen as an error in the 2D positions of the objects and of the stars, namely a segmentation error. Therefore in order to mimic such errors on the synthetic images, we add a Gaussian random noise with zero mean and given standard deviation σ to the pixel coordinates of the satellite and of the stars. In particular, we

[1] RESDOS: longitude 12°30′20″, latitude 41°57′21″, altitude 76 m; SCUDO: longitude 13°22′30″, latitude 41°45′55″, altitude 555 m

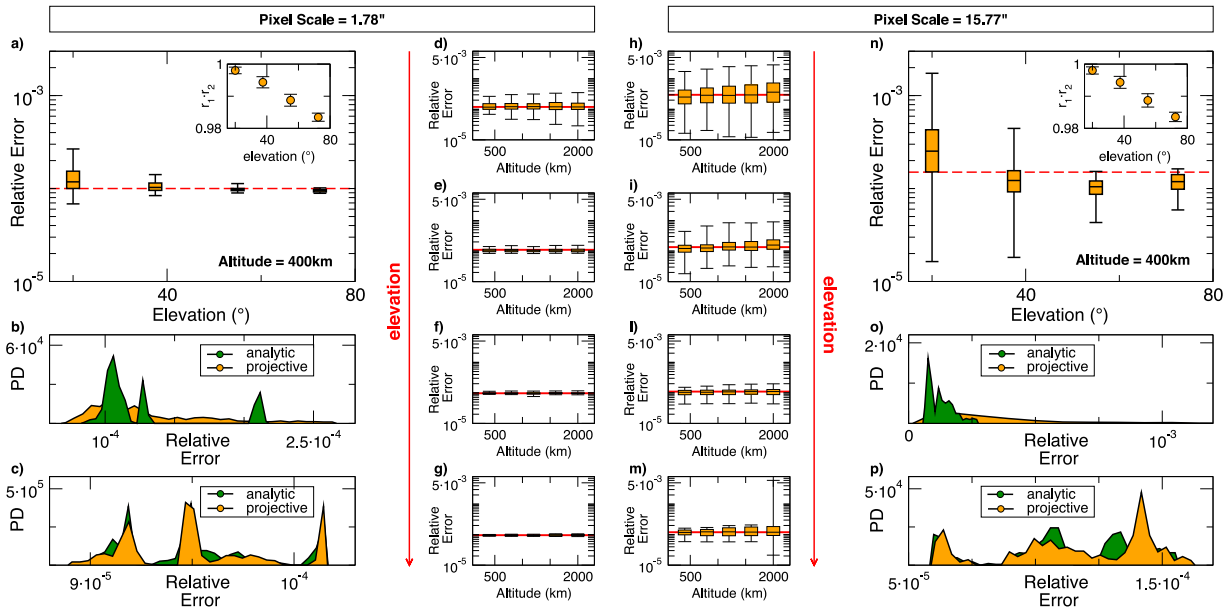

Fig. 2. Noise-free tests. In all the boxplots the line within the box represents the median value of the error distribution, the two edges of the box are the first and third quartiles and the two whiskers represent the minimum and maximum value. **First two column:** results for the synthetic data with the pixel scale equal to 1.77″ corresponding to a 750 mm focal length. **Last two column:** results for the synthetic data with the pixel scale equal to 15.77″ corresponding to a 85 mm focal length. **a and n.** The relative error obtained with the projective method as a function of the object elevation from one of the two sites at the fixed object altitude of 400 km. The relative error shows a trend with the elevation: the lower the elevation the higher the relative error. One possible reason for this trend is that the two optical rays (one for each camera) passing by the object get parallel when the elevation is low (**inset**), making the point at their intersection not well defined. **b and o.** The probability distributions of the relative error for the analytic method (green) and the projective method (orange) at the fixed elevation of 20°. The projective method shows a flatter distribution than the analytic one, suggesting that the projective method is less robust with respect to the optical rays parallelism. **c and p.** The probability distributions of the relative error for the analytic (green) and projective (orange) method at the fixed elevation of 72.5°. The two methods show comparable distributions. **d–m.** Relative error for the projective method as a function of the object altitude, from the lowest elevation (top row) to the highest elevation (bottom row). Relative error is constant with the altitude getting smaller when increasing the elevation. The comparison between the two pixel scales shows a higher error for the larger pixel scale. (For interpretation of the references to colour in this figure legend, the reader is referred to the web version of this article.)

produced synthetic data with noise in three different configurations: i. we added segmentation noise only to the $2D$ position of the satellite; ii. we added a segmentation noise only to the $2D$ position of the stars; iii. we added a segmentation error to position of both the objects and the stars.

4. Tests, validation and results

As already discussed, all the $3D$ position reconstruction tests were performed on simulated data as acquired from the two observatories in Rome and Collepardo (Italy) corresponding to a system baseline of 77 km. We produced synthetic data on virtual cameras with the characteristics of the Andor Zyla 5.5 (sensor size 16.64 mm × 14.04 mm and pixel size equal to 6.5 μm), as these are the camera currently in use in the experimental campaign. To avoid (uncontrolled) noise due to the digitization of the pixel positions of the stars and of the satellite we do not produce and analyze actual images files (namely jpg images), but we directly generate FITS (Flexible Image Transport System) files where we store the stars and objects pixel positions.

We produced synthetic data for two different configurations: the first with a small field of view (FOV) with a pixel scale of 1.78″, corresponding to a 750 mm focal length and angular FOV of 1.27 deg ×1.1 deg, and the second with a large FOV with a pixel scale of 15.77″, corresponding to a 85 mm focal length and angular FOV of 11.07 deg ×9.6 deg. The small FOV configuration is intended to simulate data collection with the telescope in object tracking mode, which is typically used to collect data of already observed objects. In contrast, the large FOV configuration is intended to simulate data collection with the telescope in sidereal tracking mode, which is typically used in sky surveillance to detect space debris that are not yet catalogued. In the following we first present the results on noise-free synthetic data, then we consider the presence of noise and finally we benchmark the methods in the case of realistic satellite passages obtained via the SPG4 propagator, as described in the previous section.

4.1. Noise-free tests

In the first set of tests we evaluate the accuracy of the two methods when the objects pixel positions of the stars and the satellite are not affected by noise. Here inaccuracy in the reconstruction comes from star annual aberration, which causes a shift of the observed position of the satellite (not affected by annual aberration) with respect to the stars and from the atmospheric refraction which, especially in the large FOV configuration, causes a nonlinear distortion (see e.g. Appendix C). In particular, refraction on the stars impacts also the accuracy of astrometrics parameter estimation.

We simulated images of simultaneous single shots of objects orbiting at different altitudes, different elevation and different azimuth coordinates. In particular, we investigate five altitude values (400 km, 800 km, 1200 km, 1600 km, 2000 km), four elevation values (20°, 37.5°, 55°, 72.5°) and six azimuth values (0°, 60°, 120°, 180°, 240°, 300°).

For each triplet altitude–elevation–azimuth we generate an image of the night stars for each site and 100 objects to be reconstructed. For each of these images we compute the object $3D$ position with both the methods. We evaluate the quality of the results comparing the reconstructed position of the object with the one used to generate the images (step 6 of the generation routine described in Section 3). Results for the two configurations with small FOV (1.78″ pixel scale) and for the large FOV (15.77″ pixel scale) are shown in Fig. 2, where we compare different configurations in terms of the relative error, defined as the ratio between the reconstructed error and the mean distance of the object range from the two observatories.

At a fixed altitude, for both methods we find a trend of the relative error with the object elevation, see Figs. 2a and 2n where we show the

results for the altitude equal to 400 km for the objects reconstructed with the projective method. Not only the error increases when the elevation decreases, but also the error fluctuations show the same trend: the lower the elevation the higher the fluctuations, and we find that the fluctuations at low elevation are higher with the projective method than with the analytic one. The main reason for such large fluctuations at low elevation is that the two optical rays (one for each camera) passing by the object are almost parallel, as demonstrated in the insets of Figs. 2a,n, where we plot the scalar product between the direction of the two optical rays ($\boldsymbol{r_1} \cdot \boldsymbol{r_2}$) as a function of the elevation. This suggests that the more the two optical rays are parallel the less effective the projective method is, see Figs. 2b, o where we compare the relative error probability distribution for the two methods at the fixed elevation of 20° while in Figs. 2c, p we show the equivalent data for elevation of 72.5°.

At a fixed elevation we find that the relative error is constant with the altitude, which implies that the absolute error gets larger when the altitude increases, see Figs. d–m. This is somehow expected as, in general, the larger the altitude the larger should be the baseline (i.e. the distance between the two observatories) to maintain the accuracy [19], while here we kept it fixed.

As expected relative errors in the small FOV configuration are lower than the ones in the large field configuration, being lower than 10^{-3} for the small FOV (corresponding to a maximum absolute error of 0.4 km for the altitude of 400 km and 2 km for the altitude of 2000 km) and lower than $2 \cdot 10^{-3}$ for the large FOV (corresponding to a maximum absolute error of 0.4 km for the altitude of 800 km and 4 km for the altitude of 2000 km). We also find that the fluctuations of the errors increases enlarging the field of view. The overall performance of the two methods is excellent with a very low relative error, with the analytic method giving better performances than the projective method when the elevation is low.

4.2. Tests with segmentation noise

This second set of tests is intended to evaluate the reconstruction error under the unavoidable segmentation noise, i.e. noise in the detection of the position of stars and objects on real images.

In these tests we simulate simultaneous single shots from the two observatories restricting our analysis to two elevation values (20° and 60°) and we compare the performance of the two methods by adding noise to the stars and objects positions on the images. The image noise is simulated by adding Gaussian noise with zero mean and three value of the standard deviation σ that expressed in pixel are chosen to be 0.5 px, 1 px and 2 px, which are in the expected range of values in real images.

We investigate three configurations: noise affecting only the objects positions, only the stars positions and finally both the stars and the objects positions. These three configurations are meant to simulate different field conditions. When we collect data with the telescope in sidereal mode we are essentially keeping the stars still with the object moving on the images, hence stars will appear as bright dots while the satellites will be bright stripes. In this specific situation, the probability of having segmentation error is higher on the satellites than on the stars. Therefore we are simulating the situation where the RA/DEC coordinates of the image center and the rotation angles γ are well calibrated, hence the geometry of the system is estimated with high accuracy while the two optical rays, on which the object lies, are corrupted by noise. On the contrary, when we collect data with the telescope in tracking mode we are essentially keeping the objects still with the stars moving on the images, hence the object appears as a bright dot while the stars as bright stripes. In this case the star-field is affected by noise, and consequently the geometry of the system is corrupted while the two optical rays are, in principle, estimated with high accuracy. Finally, in the third situation both objects and stars are affected by noise and, as a consequence, both the geometry of the system and the two optical rays are corrupted by noise.

In order to provide as strict as possible a quantitative message, we present here only the results for the worst case scenario: wide field of view (pixel scale 15.77″), segmentation error of 2 px only on the object position, only on the stars, and on both object and stars. The comparison between the reconstruction error for noisy images or noise-free images show that the addition of noise causes an important increase of the reconstruction error (compare the four columns in Fig. 3): the relative errors, which are below $2 \cdot 10^{-4}$ for noise-free images, grow from one to two orders of magnitude.

The results on the synthetic data shows that, regardless of elevation, the two methods are more robust against noise on the stars than against noise on the object position, see Fig. 3, where we compare the relative reconstruction error in the different noise conditions. The comparison between the two methods shows that in the noise-free condition, Figs. 3e and 3o, the projective method presents higher fluctuations on the relative error than the analytic method, confirming what we found in the noise-free tests presented above.

The best performance of the analytic method shown in the noise-free tests for low elevation values does not hold anymore. When the noise is added only to the object the two methods present comparable distributions, see Figs. 3f and 3p, while when the noise is added only to the stars the reprojective method shows better performance than the analytic method (a narrower probability distribution for the projective method than for the analytic method). This suggests that the projective method is more robust against noise in the estimation of the system geometry.

In the noise-free tests we show that the relative error does not depend on the altitude of the objects, see Fig. 2. Here the situation is complicated by the addition of noise, and we actually find a trend of the error with the object altitude, see Figs. 3b–d and 3l–o. The relative error gets up to 10^{-2} for objects at an altitude of 2000 km, corresponding to an absolute error of 20 km.

The comparison between the two pixel scale configurations is shown in Fig. 4, which presents the results when noise is added only on the objects. As expected, the error increases with the pixel scale (i.e. when increasing the FOV) and with a linear trend, such that increasing the pixel scale of one order of magnitude increases the relative order of one order of magnitude. The results shown in Fig. 4 suggests that in order to achieve high accuracy in the reconstruction we need a small pixel scale or equivalently a high focal length. But when increasing the focal length the field of view gets narrow, so that collecting data with telescopes in sidereal mode becomes very hard, hence unconvenient for surveillance purposes. When a sidereal system mode is preferable, higher accuracy in the $3D$ reconstruction can be achieved by increasing the system baseline, i.e. choosing different observatories at a larger mutual distance.

4.3. Tests on realistic satellites

As discussed above in order to mimic a more realistic situation we also produced images of the satellite trajectories obtained with the SPG4 propagator using the TLE released from NORAD, as described in Section 3. In particular, we considered Sentinel 2A and the ISS (International Space Station), see Table 1 for the specifications. In both cases we produced images in small and large field of view conditions. Here we present results corresponding to the worst case scenario where the elevation is low. We consider both noise-free reconstruction (only affected by stellar aberration and refraction) and noisy data build similarly to the previous case, mimicking segmentation noise on both stars and satellite with intensity 2 px. The results are shown in Table 2, where we show the average reconstruction error of the two methods over 7–10 instants of time (separated by 0.5 and 4.0 secs, respectively for small and large FOV). The error is computed as the Euclidean distance, in the J2000 reference frame, between the satellite $3D$ position

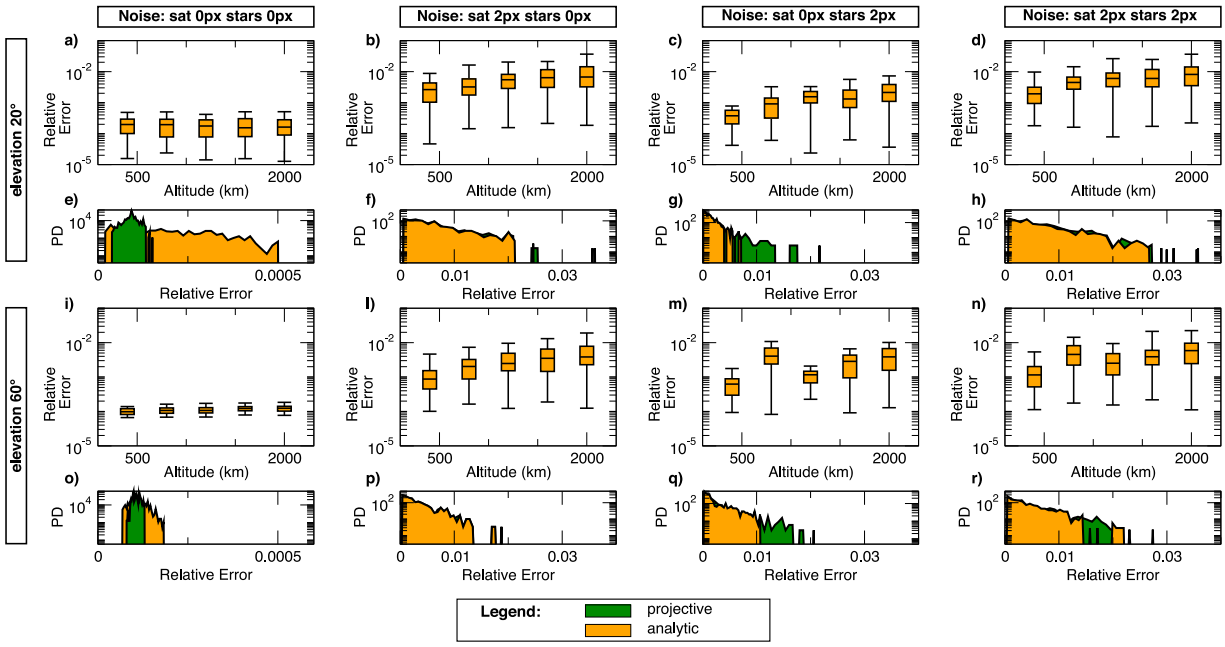

Fig. 3. Segmentation error The relative error obtained with the projective method with the addition of segmentation error to the images. **First column.** Noise-free data **Second column.** A 0 median gaussian segmentation error with $\sigma = 2$ px is added only to the image of the object. **Third column.** A 0 median gaussian segmentation error with $\sigma = 2$ px is added only to the images of the star. **Fourth column.** A 0 median gaussian segmentation error with $\sigma = 2$ px is added to the images of both the object and of the stars. **a–d** The relative error as a function of the object altitude at the fixed elevation of 20°. **e–h** The probability distributions of the relative error at the fixed elevation of 20° for the analytic (green) and projective (orange) methods. **i–m** The relative error as a function of the object altitude at the fixed elevation of 60°. **n–q** The probability distributions of the relative error at the fixed elevation of 60° for the analytic (green) and projective (orange) methods. **a–d and i–m.** The results shows that measurements are more affected by noise on the object position than on the stars positions, but also that in both cases the introduction of noise produce an increase of the relative error of almost one order of magnitude. **e–h and n–q.** In the noise free condition, the analytic method shows better performance than the projective one producing a narrower probability distribution. The introduction of segmentation noise makes the two methods comparable, with the projective method showing better performance (shorter right tail of the histogram) when the segmentation error is added to the stars position only. (For interpretation of the references to colour in this figure legend, the reader is referred to the web version of this article.)

Table 1
Satellite name, Norad number, TLE starting date, date and time of the simultaneous passage above the sites Urbe/Collepardo, altitude (in km).

Object	Norad number	TLE date	Passage	Altitude
Sentinel-2A	40697	2019/07/02 03:28:16	2019/07/02 22:07:00–22:07:36	793.96
Sentinel-2A	40697	2020/06/17 02:58:05	2020/06/16 22:10:00–22:10:36	796.19
ISS (Zarya)	25544	2020/05/20 04:32:31	2020/05/20 22:46:38–22:47:06	424.80

Table 2
Simulations: Object, date (year/month/day), pixel-scale, elevation of the center of image from the first site, average slant range of the satellite from the two sites, reconstruction error (in km) using the analytical and projective method with and without segmentation noise. Relative error (shown in parenthesis) is obtained from the absolute error dividing by the average slant range.

				Analytical		Projective	
Object	Pixel-scale	Elevation	Range	Noise-free	With noise	Noise-free	With noise
Sentinel-2A	1.78″	26.43	1528.63	0.13 (0.085‰)	1.23 (0.8‰)	0.13 (0.085‰)	1.23 (0.8‰)
Sentinel-2A	1.78″	17.63	1915.42	0.16 (0.084‰)	2.14 (1.1‰)	0.16 (0.084‰)	2.22 (1.2‰)
ISS (Zarya)	1.78″	20.31	1039.64	0.11 (0.1‰)	0.42 (0.4‰)	0.11 (0.1‰)	0.42 (0.4‰)
Sentinel-2A	15.77″	26.43	1529.19	0.26 (0.17‰)	8.77 (5.7‰)	0.25 (0.16‰)	8.82 (5.8‰)
Sentinel-2A	15.77″	16.36	1985.42	0.24 (0.12‰)	19.5 (9.8‰)	0.46 (0.23‰)	19.4 (9.8‰)
ISS (Zarya)	15.77″	19.57	1065.57	0.15 (0.14‰)	2.60 (2.4‰)	0.16 (0.15‰)	2.78 (2.6‰)

obtained by the TLE propagation, and the its $3D$ reconstructed position. Table 2 shows that the accuracy of the two methods is comparable for small FOV with the error in the range between 100 m and 200 m corresponding to a relative error (obtained dividing by the average slant range) of 0.1‰, while on large FOV 0.2‰. When segmentation noise is added, in agreement with the results of Fig. 3, the relative error grows up to 0.2–1% for large FOV while it remains in the order of 0.5–1‰ in the small FOV case. It is worth stressing that for the case of Sentinel-2A the considered baseline is somehow too small, which explains the relatively large error especially when the FOV is large.

5. Conclusions

We presented two methods for the reconstruction of the three dimensional position of space debris, via a two-site optical system. We quantified the accuracy of the two methods on synthetic data of objects orbiting around the Earth for different values of altitude (within the LEO region), elevation and azimuth, and we also investigated the role of the system focal length (which determines the field of view) in the reconstruction process. We produced synthetic data in noise-free conditions (where the only source of reconstruction inaccuracy should be due to stellar aberration and atmospheric refraction) and in the

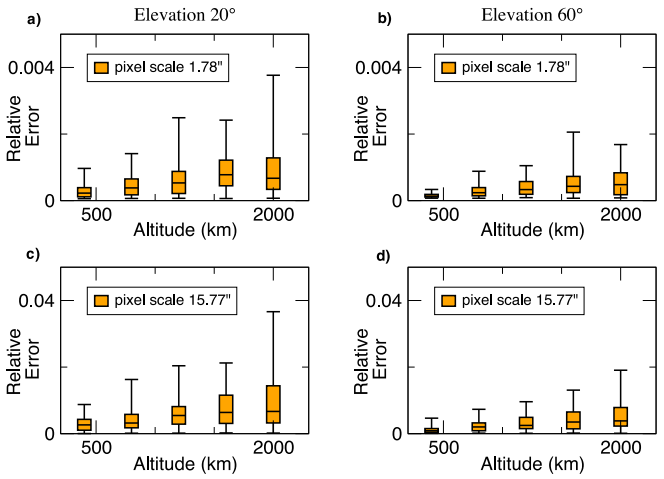

Fig. 4. Pixel scale comparison. The comparison between the relative error obtained with the projective method for the two pixel scales of 1.78″ and 15.77″ in the configuration where a noise of 2 px is added only to the object position. **First column.** The relative error as a function of the object altitude for synthetic data generated with the pixel scale of 1.78″ (top) and with the pixel scale of 15.77″ (bottom) at the fixed elevation of 20°. **Second column.** The relative error as a function of the object altitude for synthetic data generated with the pixel scale of 1.78″ (top) and with the pixel scale of 15.77″ (bottom) at the fixed elevation of 60°. For both elevation values, when increasing the pixel scale of one order of magnitude we observe an increase of the relative error of one order of magnitude. The comparison between different elevation values shows bigger error and larger fluctuations when the elevation is lower, as it happens in the noise-free simulations.

presence of segmentation error, i.e. error in the detection of the objects and of the stars on the images, here simulated as additive Gaussian noise.

The tests in noise-free condition show a reconstruction relative error that is constant with the altitude, but that shows a trend with the elevation, namely the lower the elevation the higher the reconstruction error, which is mainly due to optical rays tendency to parallelism. Tests also show that the analytic method gives a slightly better performance of the projective method for low elevation, while the two methods become comparable for medium and high values of the elevation. With the addition of the segmentation noise, the two methods give comparable results with the projecting method being more robust against noise on the position of the star, unlike the noise-free tests.

We limited the analysis to two relatively close observatories, as those sites will be soon used to make test on field data. However, the method can be extended to any couple of observatories and, of course, for far objects (beyond the LEO region) a larger baseline would be needed, i.e. the two observation sites need to be at larger distance, in order to properly reconstruct the 3D positions of the objects.

The road from synthetic to real data is quite complicated, because of the several source of errors that may affect the system hardware and software. Apart from the segmentation error, the main source of error in the case of real data is by far a potential desynchronization of the system, with the two cameras not shooting exactly at the same time. This desynchronization may originate from slight differences in the trigger signals sent to the two cameras or to different time lags at the two sites, i.e. the time needed for a camera to shoot after it receives the trigger signal. In the future we plan to conduct tests simulating a time desynchronization between the two cameras to estimate the time accuracy that we need to achieve a high accurate reconstruction.

In conclusions, while the final assessment of the method should be performed on experimental data, with the above described difficulties, we would like to stress that the potential of the methods here discussed is very high. Indeed, for instance, given the trace of an object it is in principle possible to reconstruct the 3D position of the start/end of the trace which, knowing the exposure time, can allow for providing an estimation of the 3D velocity of the object. In other terms one can, in principle, have access to the whole set of orbital parameters.

Declaration of competing interest

The authors declare that they have no known competing financial interests or personal relationships that could have appeared to influence the work reported in this paper.

Acknowledgements

We acknowledge support from grant MODSS (“Monitoring of space debris based on intercontinental stereoscopic detection”; Grant No. 85-2017-14966), a research project funded by LazioInnova/Regione Lazio according to Italian law L.R. 13/08.

Appendix A. Tools kit for the 3D reconstruction methods

The analytic and projective methods start from the same astrometric and photometric measures to define the geometry of the system. To this aim images are solved via the Open-Source library Astrometry-net, [12], to obtain the following astrometric measurements:

1. the celestial coordinates of the image center, α_0, δ_0: from the header of the FITS (Flexible Image Transport System) file we extrapolate the values corresponding to CRVAL1 and CRVAL2 respectively.
2. the scale and rotation matrix, CD, which includes information on:
   (a) the angle, γ that measures the sensor rotation with respect to the Celestial North (see also Appendix D);
   (b) the system scale factor expressed in arsec/px;
3. the distortion SIP (Simple Image Polynomial) parameters.

A.1. Analytic method

First we associate to each pixel its J2000 topocentric celestial coordinates, α_T and δ_T, through the Open-Source library Astropy [20,21], which uses the two angles α_0 and δ_0, the matrix CD and the SIP distortion parameters defined above, [22,23]. Second we convert the geographic coordinates of the two observation sites (latitude, longitude and altitude) to the J2000 reference frame. Finally we define the two optical rays as:

$$r_1 : \begin{cases} X = X_0 + lt \\ Y = Y_0 + mt \\ Z = Z_0 + nt \end{cases} \qquad r_2 : \begin{cases} X = X'_0 + l't' \\ Y = Y'_0 + m't' \\ Z = Z'_0 + n't' \end{cases} \tag{A.1}$$

where (X_0, Y_0, Z_0) and (X'_0, Y'_0, Z'_0) represent the J2000 coordinates of the two observation sites, (l, m, n) and (l', m', n') are the versor of the two optical rays defined from the topocentric coordinates of the objects. Namely:

$$\begin{cases} l = \cos\alpha_T \cos\delta_T \\ m = \sin\alpha_T \cos\delta_T \\ n = \sin\delta_T \end{cases} \qquad \begin{cases} l' = \cos\alpha'_T \cos\delta'_T \\ m' = \sin\alpha'_T \cos\delta'_T \\ n' = \sin\delta'_T \end{cases} \tag{A.2}$$

The point at the intersection between the two lines is then defined as the point closest to both the lines and it is found with a least-square approach, [9].

A.2. Projective method

For the projective method, we start by extrapolating γ from the CD matrix in the following way:

$$\gamma = \text{atan}((CD_{21} - CD_{12})/(CD_{11} + CD_{22})) \tag{A.3}$$

where CD_{ij} is the element on the ith row and jth column of the matrix CD.

Then we rotate the pixel coordinates around the image center of $-\gamma$. More in detail, given the pixel coordinates, u and v, of a point $s = (u, v)$ and the pixel coordinates of the image center (u_0, v_0) we obtain the counter rotated point $\bar{s} = (\bar{u}, \bar{v})$:

$$\begin{pmatrix} \bar{u} \\ \bar{v} \end{pmatrix} = \begin{pmatrix} u_0 \\ v_0 \end{pmatrix} + \begin{pmatrix} \cos\gamma & \sin\gamma \\ -\sin\gamma & \cos\gamma \end{pmatrix} \begin{pmatrix} u - u_0 \\ v - v_0 \end{pmatrix} \tag{A.4}$$

where the pixel coordinates are expressed in the image reference frame, with the origin in the top left corner, the u-axis pointing right and the v-axis pointing down. Note that the image center is not the origin of this system, hence $(u_0, v_0) \neq (0, 0)$. For the sake of simplicity in the notation, in the following we will refer to $(\bar{u}, \bar{v})$ as (u, v).

The projective method uses the formalism of projective geometry and the pinhole model, [9]. In such formalism the position of a $3D$ object, S, and its $2D$ image, s, are related by:

$$\hat{s} = P \cdot \hat{S} \tag{A.5}$$

where $\hat{s} = (\hat{u}, \hat{v}, \hat{w})$ represents the projective coordinates of the $2D$ point $s = (u, v)$, i.e. s and $\hat{s}$ are such that $u = \hat{u}/\hat{w}$ and $v = \hat{v}/\hat{w}$, $\hat{S} = (\hat{X}, \hat{Y}, \hat{Z}, \hat{W})$ represents the projective coordinates of the $3D$ point $S = (X, Y, Z)$, i.e. S and $\hat{S}$ are such that $X = \hat{X}/\hat{W}$, $Y = \hat{Y}/\hat{W}$ and $Z = \hat{Z}/\hat{W}$, and P represent the 3×4 projective matrix that define the geometry of the system, [9].

The projective matrix is given by the composition of three matrices:

$$P = K[R|T] \tag{A.6}$$

where K is the 3×3 matrix of the intrinsic parameters, R is the 3×3 rotation matrix R and T is the three dimensional translational vector.

The matrix of the intrinsic parameters K is defined as:

$$K = \begin{pmatrix} \Omega_x & 0 & u_0 \\ 0 & \Omega_y & v_0 \\ 0 & 0 & 1 \end{pmatrix} \tag{A.7}$$

where (u_0, v_0) are the pixel coordinates of the image center, Ω_x and Ω_y are the camera focal length on the x and y axis with $\Omega_x = C/scaleFactor_x$ and $\Omega_y = C/scaleFactor_y$, with C being a conversion factor from arcsec to rad and:

$$\begin{cases} scaleFactor_x = \sqrt{CD_{11}^2 + CD_{21}^2} \\ scaleFactor_y = \sqrt{CD_{12}^2 + CD_{22}^2} \end{cases} \tag{A.8}$$

where CD_{ij} is the element on the ith row and jth column of the matrix CD.

R and T represent the rotational matrix and the translational vector that bring the camera reference frame,[2] in the world reference frame. We determine R from the celestial coordinates of the image center and T from the GPS coordinates of the observation site.

In particular, given the ra/dec coordinates of the image center, (α_0, δ_0), the rotation matrix is defined as:

$$R = R^* \cdot R_y(\pi/2 - \delta_0) \cdot R_z(-\alpha_0) \tag{A.9}$$

[2] The $3D$ reference frame $OXYZ$ with the origin in the camera optical center, the XY-plane parallel to the sensor with the X-axis pointing right and the Y-axis pointing down and the Z-axis oriented as the camera optical axis

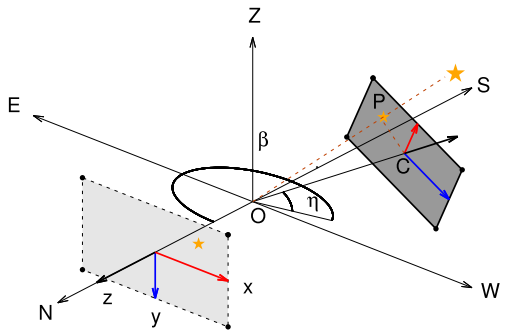

Fig. B.5. Schematic sketch of the sensor positioning and the projection scheme. The light gray shaded rectangle represents the sensor placed at zero azimuth and elevation with attached the optical frame of reference (x, y, z). The origin O represents the optical center of the camera and the distance between origin and the sensor the focus length f. The origin lies on a plane parallel to that tangent to the Earth surface, whose axis are denoted with the cardinal directions N, S, W, E while the axis perpendicular to the horizon is denoted with Z (Zenith). The dark gray rectangle represents the sensor rotated to point to the desired azimuth and elevation on the sky. The point P (denoted with a yellow star) is the projection of the celestial or orbiting object S on the rotated sensor, and the yellow star on the light gray rectangle its position in the original position of the sensor, whose (x, y) coordinates corresponds to the position of the object S in the final image. The algebra used to perform the projection is described in the text.

where $R_z(-\alpha_0)$ is a rotation about the z-axis of the angle $-\alpha_0$, $R_y(\pi/2 - \delta_0)$ is a rotation about the y-axis of the angle $\pi/2 - \delta_0$, and

$$R^* = \begin{pmatrix} 0 & -1 & 0 \\ 1 & 0 & 0 \\ 0 & 0 & 1 \end{pmatrix} \tag{A.10}$$

which is needed to take care of the different orientation between the camera reference frame and the world reference frame.

The translational vector is defined from the J2000 coordinates of the observation site as $T = (-X_0, -Y_0, -Z_0)$, where the negative sign is needed because T defines the vector that brings the observation site into the origin of the world reference frame.

Once the projective matrices are defined for both sites, in the projective method we find the $3D$ position of the object solving the following linear system, in the unknown S:

$$\begin{cases} \hat{s} = P\hat{S} \\ \hat{s}' = P'\hat{S} \end{cases} \tag{A.11}$$

where $\hat{s}$ and $\hat{s}'$ are the projective coordinates of the $2D$ images of the object on the two sensors and P and P' are the two projective matrices. We solve the system with a standard approach in the field of computer vision: the DLT approach (direct linear triangulation [9]).

Appendix B. Projection of an object on the sensor given its azimuth and elevation

In building the image we assume the sensor to have a rectangular shape with sides a and b and we consider the focal distance to be f. In our tests, these parameters are set as $f = 750$ mm, $a = 16.64$ cm, $b = 14.04$ cm.

Given the azimuth and (apparent) elevation of the sensor center and those of any object to be projected on the sensor the procedure we followed depicted in Fig. B.5. We denote with $\{x, y, z\}$ the frame of reference of the camera, (x_P, y_P) will be the position of the projection of the object on the image, and with capital letter the "topocentric" (SEZ) reference frame, for the latter the we consider the cardinal directions and the Zenith. Placing the sensor the normal unit vector $\hat{z}$ pointing towards the north (see the dashed light gray rectangle), x axis oriented towards West and y axis pointed into the ground (Nadir). In order to determine (x_P, y_P), we first rotate the sensor so that the segment $\overline{OC}$, connecting the origin with the center of the sensor points in a

desired direction (see dark gray rectangle). Denoting with (β_0, η_0) the desired direction of the optical axis, such rotation is realized via the transformation

$$\mathbb{R} = \mathbb{R}_W(-\eta_0)\mathbb{R}_Z(-\beta_0)\,. \tag{B.1}$$

Then we determine the position of the projection P as a 3D position lying on the sensor plane. This is realized as follows. Given the azimuth and elevation (β, η) of the object to be projected the light ray connecting it to O has direction $\widehat{OP} = (\cos\beta\cos\eta, -\sin\beta\cos\eta, \sin\eta)$. Thus the only unknown quantity is the modulus of $|\overline{OP}|$ which identifies the intersection with the plane of the sensor. The latter can be determined as

$$\overline{OP} = \frac{|OC|}{\cos\theta}\widehat{OP} \tag{B.2}$$

with $\cos\theta = \widehat{OC}\cdot\widehat{OP}$ being the angle between the center and the object unit vectors. As for the segment $\overline{OC}$, connecting the origin with the center of the sensor, it has modulus $|OC|$ equal to the focal length f and unit vector given by $\widehat{OC} = (\cos\beta_0\cos\eta_0, -\sin\beta_0\cos\eta_0, \sin\eta_0)$. Once the 3D coordinates of P are known, it is sufficient to apply the rotation (B.1) in reverse order to obtain the two-dimensional coordinates (x_P, y_P) on the image.

Appendix C. Atmospheric refraction

The apparent elevation of an object due the effect of atmospheric refraction is well approximated by the formula [16]:

$$\eta' = \eta + \frac{1.02}{60.\tan\left(\eta + \frac{10.3}{\eta + 5.11}\right)} \tag{C.1}$$

where η is the true elevation (expressed in degrees).

Note that in Eq. (C.1), the temperature is fixed at 10 °C and the pressure at 1010 mbar and it refers to the yellow light only.

Refraction can modify the projection of the object on the sensor and such effect is larger at low elevations. In Fig. C.6, we show the color map of such change in pixel. At low elevation of the center, the pattern of refraction is formed by the horizontal stripes. The displacement is constant along the x axis and it increases along the y axis. Pointing at higher elevation towards the zenith of the observer, the horizontal bands changes into elongated ellipses (which become perfect circles for $\eta_c = 90°$). In this case, the error is minimum at the center and it increases radially.

Averaging over all the pixels of the sensor, the mean error can be studied as a function of the elevation of the center, as reported in Fig. C.6. For elevation $\eta_c > 20°$, we obtain that the correction due to refraction is smaller than one pixel.

Appendix D. Orientation angle

Consider the unit vector pointing at an object in the sky $\boldsymbol{R}$ and the orthogonal directions $\boldsymbol{E}$ and $\boldsymbol{S}$, pointing towards the local East and South, respectively, defined as

$$\boldsymbol{E} = \frac{\boldsymbol{K}\wedge\boldsymbol{R}}{|\boldsymbol{K}\wedge\boldsymbol{R}|}, \qquad \boldsymbol{S} = \boldsymbol{E}\wedge\boldsymbol{R}. \tag{D.1}$$

We denotes the triad of unit vectors with the label $\boldsymbol{W} = (\boldsymbol{R}, \boldsymbol{E}, \boldsymbol{S})$. In equatorial coordinates, using right ascension α and declination δ, such vector are given by

$$\boldsymbol{W} = \begin{pmatrix} \cos\delta\cos\alpha & \cos\delta\sin\alpha & \sin\delta \\ -\sin\delta & \cos\alpha & 0 \\ \cos\delta\cos\alpha & \sin\delta\sin\alpha & -\cos\delta \end{pmatrix} \tag{D.2}$$

which can be expressed in terms of the azimuthal coordinates (β, η) and given the geographical longitude λ and latitude ϕ. Using [11]

$$\begin{aligned} \delta &= \mathrm{asin}\left(\sin\eta\sin\phi + \cos\eta\cos\phi\cos\beta\right), \\ \alpha &= \lambda - \mathrm{atan}\left(\frac{\sin\beta\cos\eta\cos\phi}{\sin\eta - \sin\phi\sin\delta}\right) \end{aligned} \tag{D.3}$$

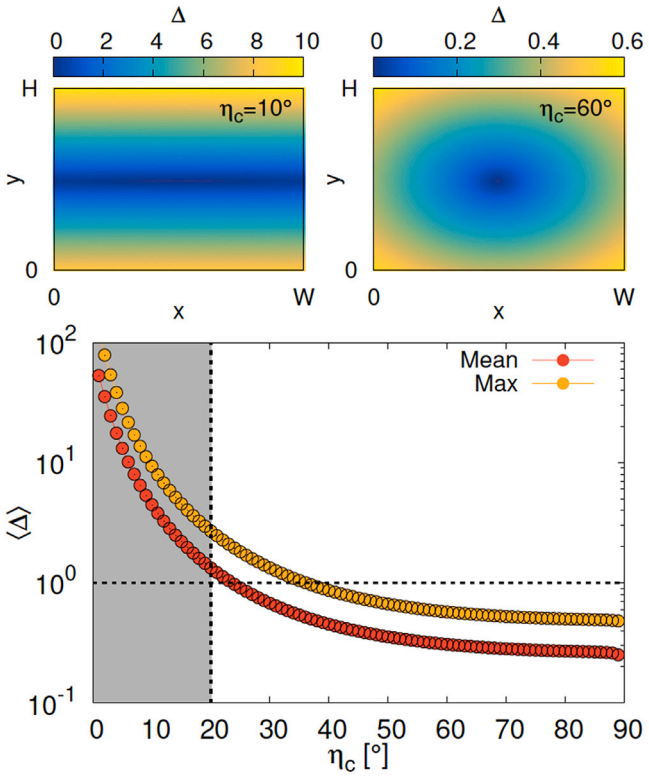

Fig. C.6. Color map of the correction Δ due to refraction in terms of pixels and mean error $\langle\Delta\rangle$. (For interpretation of the references to colour in this figure legend, the reader is referred to the web version of this article.)

The transformation from azimuthal (SEZ) to equatorial (TEQ) coordinates is given by

$$\mathbb{P} = \mathbb{R}_z(\delta)\,\mathbb{R}_y\left(\frac{\pi}{2} - \alpha\right) \tag{D.4}$$

The inverse transformation (i.e. from TEQ to SEZ) is obtained using the transpose matrix $\mathbb{P}^T$. The rotation matrix for the sensor is given by

$$\mathbb{Q} = \mathbb{R}_z(-\beta)\,\mathbb{R}_y(\eta) \tag{D.5}$$

where β is the azimuth and η is the elevation of the object.

We transform the triad of unit vectors $\boldsymbol{W}$ from equatorial to azimuthal coordinates $\boldsymbol{W}_{sez} = \mathbb{P}^T\boldsymbol{W}_{teq}$ Then, we project $\boldsymbol{W}$ onto the sensor plane $\boldsymbol{W}'_{sez} = \boldsymbol{W}_{sez} - (\boldsymbol{R}_{sez}\cdot\boldsymbol{W}_{sez})\boldsymbol{R}_{sez}$ Finally we apply the rotation $\boldsymbol{W}''_{sez} = \mathbb{Q}^T\boldsymbol{W}'_{sez}$. The orientation angle γ of the sensor with respect to the equatorial frame of reference is defined as $\gamma = \mathrm{atan}\left(S''_2/S''_3\right) = \mathrm{atan}\left(E''_3/E''_2\right)$ which gives

$$\gamma = \mathrm{atan}\left(\frac{\cos\phi\sin\beta}{\cos\eta\sin\phi - \cos\beta\cos\phi\sin\eta}\right) \tag{D.6}$$

References

[1] C. Contant-Jorgenson, P. Lála, K.-U. Schrogl, The iaa cosmic study on space traffic management, Space Policy 22 (4) (2006) 283–288, http://dx.doi.org/10.1016/j.spacepol.2006.08.004.

[2] T. Schildknecht, U. Hugentobler, M. Ploner, Optical surveys of space debris in geo, Adv. Space Res. 23 (1) (1999) 45–54, http://dx.doi.org/10.1016/S0273-1177(98)00229-4.

[3] M. Porfilio, F. Piergentili, F. Graziani, The 2002 Italian optical observations of the geosynchronous region, Adv. Astronaut. Sci. 114 (2003) 1237–1252.

[4] Skolnik M.I., Introduction to radar systems, third ed., in: McGraw-Hill International Editions. Electrical Engineering Series, McGraw-Hill, 2001.

[5] F. Piergentili, R. Ravaglia, F. Santoni, Close approach analysis in the geosynchronous region using optical measurements, J. Guid. Control Dyn. 37 (2) (2014) 705–710, http://dx.doi.org/10.2514/1.59821.

[6] M. Porfilio, F. Piergentili, F. Graziani, Two-site orbit determination: The 2003 geo observation campaign from Collepardo and Mallorca, Adv. Space Res. 38 (9) (2006) 2084–2092.
[7] V.T.R. Danescu, F. Oniga, O. Cristea, Long baseline stereovision for automatic detection and ranging of moving objects in the night sky, Sensors 12 (10) (2012) 12940–12963.
[8] R. Danescu, A. Ciurte, F. Oniga, O. Cristea, P. Dolea, V. Dascal, V. Turcu, L. Mircea, D. Moldovan, Surveillance of medium and high earth orbits using large baseline stereovision, AIP Conf. Proc. 1634 (1) (2014) 144–150.
[9] R.H.A. Zisserman, Multiple View Geometry in Computer Vision, Cambridge University Press, 2004.
[10] S. Hadji Hossein, M. Acernese, T. Cardona, G. Cialone, F. Curianò, L. Mariani, V. Marini, P. Marzioli, L. Parisi, F. Piergentili, F. Santoni, Sapienza space debris observatory network (sson): A high coverage infrastructure for space debris monitoring, J. Space Saf. Eng. 7 (12) (2019) http://dx.doi.org/10.1016/j.jsse.2019.11.001.
[11] Vallado D.A., Fundamentals of Astrodynamics and Applications, Vol. 12, Springer Science & Business Media, 2001.
[12] D. Lang, D.W. Hogg, K. Mierle, M. Blanton, S. Roweis, Astrometry.net: Blind astrometric calibration of arbitrary astronomical images, Astron. J. 139 (5) (2010).
[13] Celestrak, 1985, https://celestrak.com/.
[14] E. Hog, C. Fabricius, V.V. Makarov, S. Urban, T. Corbin, G. Wycoff, U. Bastian, P. Schwekendiek, A. Wicenec, The Tycho-2 Catalogue of the 2.5 Million Brightest Stars, Tech. rep., Naval Observatory, Washington DC, 2000.
[15] Tycho-2 catalogue data files, 2000, http://archive.eso.org/ASTROM/TYC-2/data/. (Accessed 12 April 2021).
[16] Meeus J., Astronomical Algorithms, Willmann-Bell Richmond, 1991.
[17] R.C. Stone, An accurate method for computing atmospheric refraction, Publ. Astron. Soc. Pac. 108 (729) (1996) 1051–1058.
[18] J. Gubler, D. Tytler, Differential atmospheric refraction and limitations on the relative astrometric accuracy of large telescopes, The Publications of the Astronomical Society of the Pacific 110 (748) (1998) 738–746.
[19] A. Cavagna, C. Creato, L. Del Castello, I. Giardina, S. Melillo, L. Parisi, M. Viale, Error control in the set-up of stereo camera systems for 3D animal tracking, Eur. Phys. J. Spec. Top. 224 (17) (2015) 3211–3232.
[20] Astropy Collaboration, T.P. Robitaille, E.J. Tollerud, P. Greenfield, M. Droettboom, E. Bray, T. Aldcroft, e.a. Davis, Astropy: A community Python package for astronomy, Astron. Astrophys. 558 (2013).
[21] Astropy Collaboration, A.M. Price-Whelan, B. Sipőcz, H. Günther, P. Lim, S. Crawford, S. Conseil, D. Shupe, M. Craig, N. Dencheva, A. Ginsburg, et al., The astropy project: Building an open-science project and status of the v2.0 core package, Astron. J. 156 (3) (2018).
[22] E. Greisen, M. Calabretta, Representations of world coordinates in fits, Astron. Astrophys. 395 (2002) 1061–1075.
[23] M.R. Calabretta, F. Valdes, E.W. Greisen, S.L. Allen, Representations of distortions in FITS world coordinate systems, in: F. Ochsenbein, M.G. Allen, D. Egret (Eds.), Astronomical Data Analysis Software and Systems, ADASS XIII, in: Astronomical Society of the Pacific Conference Series, vol. 314, 2004, p. 551.